Enhancing surface plasmon polariton propagation lengths via coupling to asymmetric waveguide structures

Jason M. Montgomery and Stephen K. Gray
Chemical Sciences and Engineering Division and Center for Nanoscale Materials, Argonne National Laboratory, Argonne, Illinois 60439, USA

(Received 27 November 2007; revised manuscript received 24 January 2008; published 10 March 2008)

We determine and analyze the properties of regenerated surface plasmon polaritons (R-SPPs) in an asymmetric waveguide structure [T.-W. Lee and S. K. Gray, Appl. Phys. Lett. **86**, 141105 (2005)]. Both finite-difference time-domain (FDTD) calculations and frequency-domain modal analysis are employed. The FDTD results, which explicitly include excitation via attenuated total reflection, show an oscillatory dependence of the R-SPP propagation length L_x as a function of core layer thickness d, with maxima corresponding to 30-fold propagation enhancements. For fixed incident light wavelength and angle, a variety of thicknesses can therefore be used to excite very long propagating SPPs. Modal analysis shows that the oscillations are due to tuning d through the opening of new transverse magnetic waveguide modes. In addition to increased propagation lengths, surface confinement is not significantly deteriorated and large intensity enhancements in the propagation region can also be achieved.

DOI: 10.1103/PhysRevB.77.125407 PACS number(s): 73.20.Mf, 78.20.Bh, 71.36.+c, 42.79.Gn

I. INTRODUCTION

Surface plasmon polaritons (SPPs) are propagating electromagnetic surface waves that are evanescently confined to a metallic surface.[1] When efficiently excited, SPPs can also be intense relative to the incident light. These properties make them attractive for use in a range of applications. For example, they form the basis for some chemical and biological sensing devices,[2–4] and a variety of other possibilities in spectroscopy, telecommunication, imaging, and device physics are actively being explored.[5–7] For many of these applications, the SPP propagation length L_x on the surface should be as long as possible.

One approach to lengthening L_x is to couple the SPP into a waveguide structure. Several waveguide structures have been proposed in the literature, e.g., Refs. 8–11. Sarid's pioneering work in 1981 introduced the idea of a long range surface plasmon polariton (LR-SPP) mode that propagates on a thin metal film sandwiched between two dielectric layers with similar refractive indices.[8] Propagation lengths of more than an order of magnitude longer compared to isolated SPP values were predicted. In general, optimum results occur when the refractive indices of the lower and upper dielectric media are equal or close in value to reduce radiation loss, and the metal film is as thin as can be reasonably achieved to reduce absorption loss. Early experimental validation of the LR-SPP idea used a frustrated total internal reflection coupler to excite the mode.[12] Other experimental demonstrations[13,14] have used end-fire excitation.[15]

As noted above, LR-SPPs are generally discussed in the context of symmetric or almost symmetric dielectric layer claddings of the metal film. In this limit and for thin metal films, the system has two transverse magnetic (TM) modes that involve plasmons: a symmetric mode and an antisymmetric mode. Here, the symmetry is defined with respect to the transverse magnetic field component inside the metal film, i.e., the symmetric mode has no node and the antisymmetric mode has one node in this component. (In this case, the transverse electric field is proportional to the transverse magnetic field and so has the same symmetry.[15]) The LR-SPP, with this convention, is the even mode.

It is also possible to enhance SPP propagation lengths using more asymmetric waveguide structures.[9,10] For example, consider the structure in the top panel of Fig. 1, which was suggested by Lee and Gray in Ref. 9. The struc-

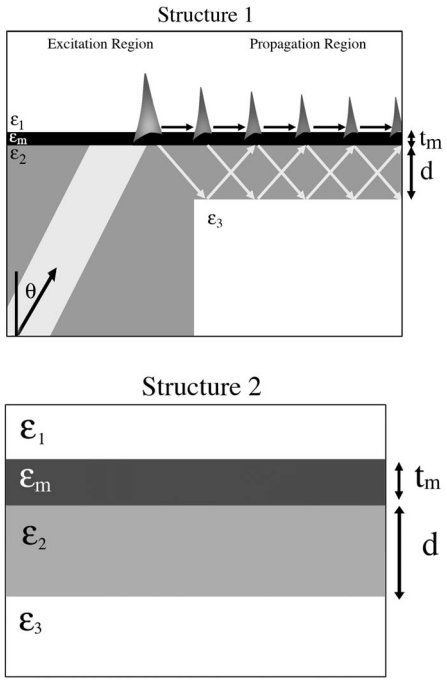

FIG. 1. The two structures considered. Structure 1 is the R-SPP structure of Ref. 9 and structure 2 is a four-layer slab waveguide. Layers 1, 2, and 3 are dielectric materials with dielectric constants ε_1, ε_2, and ε_3. The thickness of dielectric layer 2 underneath the metal, d, is a key variable. Between layers 2 and 3, there is a thin metal film of thickness t_m and frequency-dependent, complex dielectric constant ε_m.

ture includes a natural excitation region (left-hand side) where an efficient Kretschmann–Raether attenuated total reflection (ATR) approach[1] can be used if the dielectric layers satisfy $\varepsilon_2 > \varepsilon_1$ [and of course, for the incident wavelength considered, $\mathrm{Re}(\varepsilon_m) < 0$]. The essence of the idea is that ATR excitation creates SPPs at the layer 1/metal interface, which enter into the propagation region (right-hand side of Fig. 1) where now there is an additional dielectric layer 3 with $\varepsilon_3 < \varepsilon_2$. Layer 2, just under the metal, will also be referred to as the core layer. If the core layer thickness d was infinite, one would have the standard picture of SPP excitation and propagation on a metal film sandwiched between higher index material 2 (e.g., a glass prism) and lower index material 1 (e.g., air). In such a situation, the SPP is allowed to radiate into the higher index material leading to loss. However, for finite d, total internal reflection occurs at the 2/3 interface, and this sends back what would be SPP radiation loss up to the metal surface at just the right angle to regenerate SPPs. This was termed a regenerated surface plasmon polariton (R-SPP) structure.[9] For silver films on glass ($\varepsilon_2 = 2.25$) with air for layers 1 and 3, it was found that *small* core (glass) and metal film thicknesses (e.g., $d = t_m = 30$ nm) yielded the most dramatic enhancements.

The purpose of this paper is to show that very similar increases in propagation lengths and intensity enhancements can be obtained with a variety of much larger values of glass core thickness d, which may make the approach more amenable to experimental verification and device applications. We also show how this can be explained physically in terms of efficient coupling into certain waveguide modes. Our work involves both full finite-difference time-domain (FDTD) calculations,[9,16] which include a realistic model of the ATR excitation process, and extensive frequency-resolved modal calculations based on Yeh's matrix approach.[17]

Section II is a brief description of the theoretical methods employed, Sec. III contains our results and analysis, and Sec. IV concludes. The Appendix gives additional details of the modal calculations.

II. THEORETICAL METHODS AND COMPUTATIONAL DETAILS

We consider the layered waveguide structures given in Fig. 1. Structure 1 is the original R-SPP configuration of Ref. 9, and structure 2 is a simpler slab waveguide system. Both structures are invariant along z, and the focus is on SPP generation and propagation at layer 1 and/or metal interface. The calculations we present correspond to dielectric constants $\varepsilon_1 = \varepsilon_3 = 1.0$ (air), $\varepsilon_2 = 2.25$ (glass), $\varepsilon_m = \varepsilon_{\mathrm{Ag}}(\omega) = \varepsilon'_{\mathrm{Ag}}(\omega) + i\varepsilon''_{\mathrm{Ag}}(\omega)$ (silver at a given optical frequency ω), and $t_m = 30$ nm, although other materials and metal thicknesses are certainly possible.

A. Finite-difference time-domain calculations

We carry out FDTD calculations for the R-SPP system, structure 1 of Fig. 1, which indicate not only how SPP propagation properties are altered by the underlying dielectric layers but also how light is coupled into the structure. For p-polarized incident light, the symmetry is such that the relevant first-order time-domain Maxwell's equations involve three coupled field components, $E_x(x,y,t)$, $E_y(x,y,t)$, and $H_z(x,y,t)$.[18]

The FDTD calculations are similar to those described in Ref. 9. A total-field and/or scattered-field approach[16] is used to introduce an incident beam that has a sinusoidal time dependence with angular frequency ω_0, corresponding to wavelength $\lambda_0 = 2\pi c/\omega_0 = 532$ nm. The beam is incident on the metal film from the glass side at an angle θ, as indicated in structure 1 of Fig. 1, and has a 4 μm Gaussian spatial profile transverse to its propagation direction. We take $\theta = \theta_{\mathrm{SPP}} = 44.6°$, where θ_{SPP} is an estimate of the angle for light to efficiently couple into SPPs on the Ag and/or air interface via momentum matching. From Ref. 1,

$$\theta_{\mathrm{SPP}} = \sin^{-1}\{[\varepsilon'_{\mathrm{Ag}}\varepsilon_1/\varepsilon_2(\varepsilon'_{\mathrm{Ag}} + \varepsilon_1)]^{1/2}\}. \tag{1}$$

Auxiliary differential equations[16,18] are introduced into the FDTD scheme to be consistent with a Drude model for $\varepsilon_{\mathrm{Ag}}(\omega)$,

$$\varepsilon_{\mathrm{Ag}}(\omega) = \varepsilon_\infty - \frac{\omega_D^2}{\omega^2 + i\Gamma_D\omega}, \tag{2}$$

where $\varepsilon_\infty = 4.1683$, $\omega_D = 1.3402 \times 10^{14}$ Hz, and $\Gamma_D = 2.1264 \times 10^{14}$ Hz. At $\omega = \omega_0$ corresponding to $\lambda_0 = 532$ nm, $\varepsilon_{\mathrm{Ag}} = -10.1 + i0.84$, compared to the experimental value $\varepsilon_{\mathrm{Ag}}^{\mathrm{expt.}} = -10.55 + i0.84$.[19]

A staggered FDTD x-y grid is used, with x ranging from 0 to 30 μm and y ranging from 0 to 6 μm, with a 0.005 μm=5 nm grid spacing in each dimension. The silver layer is placed at $y = 4$ μm. Each simulation runs for 160 fs with a time step of 0.011 fs. A uniaxial perfectly matched layer is implemented to absorb field components near the grid boundaries.[16] Each FDTD simulation requires approximately 137 min on a 2.16 GHz Intel Core 2 Duo MacBook Pro laptop computer.

The propagation time of 160 fs, with the continuous wave incident light beam, is sufficiently long to generate a "steady state" corresponding to the incident frequency ω_0. In FDTD calculations, this means that the (real) electric field vector, $\mathbf{E}(x,y,t)$, varies in a time-repetitive manner according to $\mathbf{E}(x,y,t) = \mathrm{Re}\{\mathbf{E}^c(x,y)\exp(-i\omega_0 t)\}$, where $\mathbf{E}^c(x,y) = \hat{\mathbf{x}}E_x^c(x,y) + \hat{\mathbf{y}}E_y^c(x,y)$ is the frequency-domain, complex phasor solution to Maxwell's equations consistent with the incident wave. If one has SPP propagation near the layer 1/metal interface, both the transverse (E_y^c) and longitudinal (E_x^c) phasor components will, for a fixed y just above the metal surface, vary in x according to $\exp(ik_x x)$, where the propagation constant, k_x is complex, $k_x = \beta + i\alpha$. The imaginary component α corresponds to an absorption of energy by the metal and gives rise to an exponential decrease in the electric field intensity for increasing x,

$$|\mathbf{E}|^2 \propto \cos^2(\beta x - \omega_0 t + \varphi)\exp(-x/L_x), \tag{3}$$

where $L_x = 1/2\alpha$ and φ is a phase factor. For a fixed vertical distance above the metal film, we determine L_x by examining

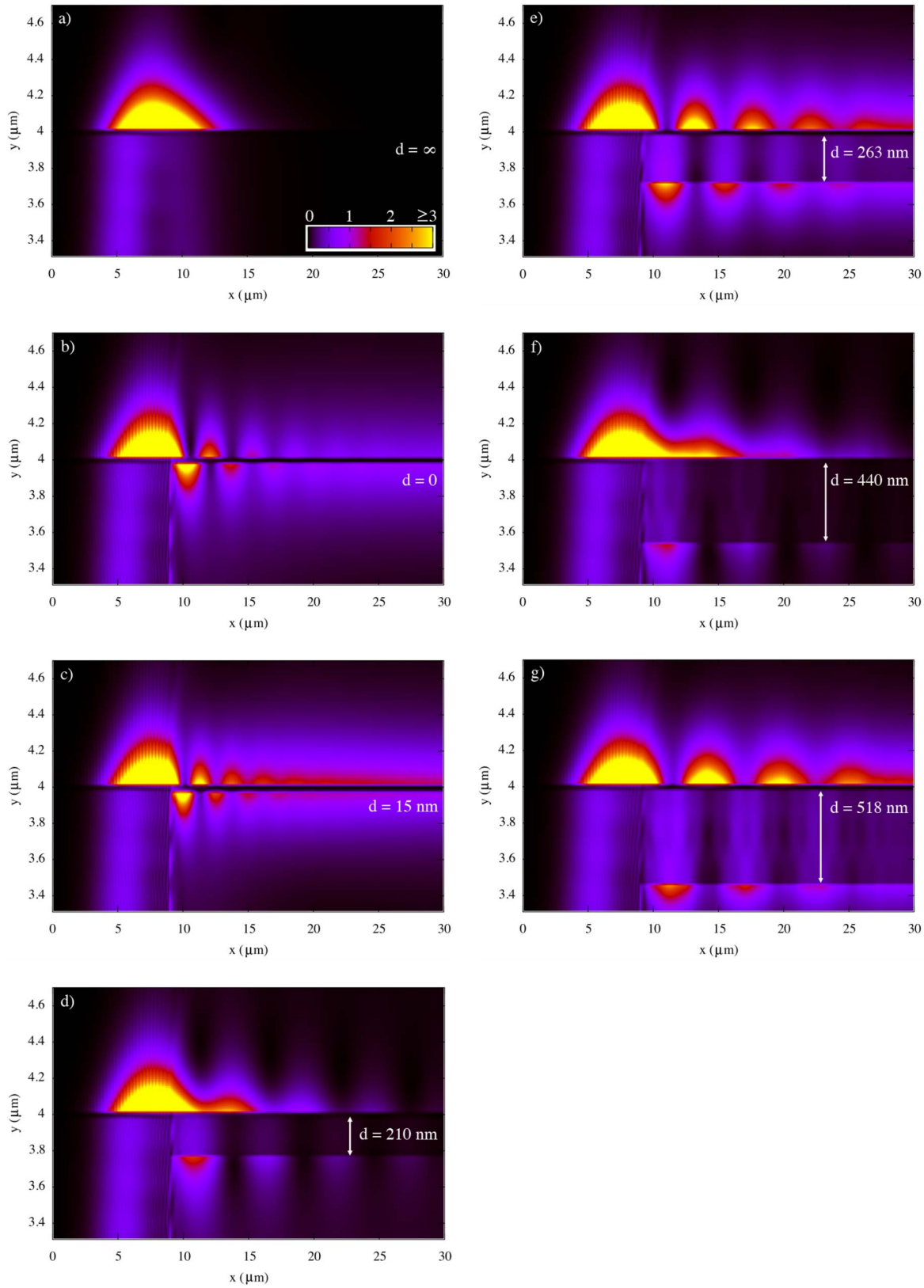

FIG. 2. (Color online) FDTD results for the time-averaged electric field intensities for structure 1 in Fig. 1 for (a) $d=\infty$ (conventional ATR), (b) $d=0$ nm, (c) $d=15$ nm, (d) $d=210$ nm, (e) $d=263$ nm, (f) $d=440$ nm, and (g) $d=518$ nm. Only the region between $y=3.3$ and 4.7 μm is shown. In each case, the incident field intensity is given by $\langle E_{\mathrm{inc}}^2\rangle_t=0.5$ V^2/m^2, and the maximum field intensity occurs in the excitation region near $x=7$ μm, for which $\langle E^2\rangle_t=10$ V^2/m^2. However, intensities ≥ 3 V^2/m^2 are represented by yellow, as indicated in (a).

the x variation of the time-averaged FDTD intensity $\langle|\mathbf{E}|^2\rangle_t$, given by

$$\langle|\mathbf{E}|^2\rangle_t = \frac{1}{T}\int_{\tau}^{\tau+T} |\mathbf{E}|^2 dt, \tag{4}$$

where τ is sometime in the steady-state limit and $T=2\pi/\omega_0$. If Eq. (3) holds, then Eq. (4) should decay exponentially in x. We therefore determine L_x by fitting the FDTD time-averaged intensity to $C\exp(-x/L_x)$. We use a fixed y corresponding to 17 nm above the metal and/or air interface and carry out the fits in the propagation region ($x>10$ μm). Whereas Ref. 9 focused on relatively small values of glass thickness d below the silver layer, we determine L_x from separate FDTD calculations covering a wide range of d values from $d=25$ to 625 nm.

B. Modal calculations

The propagation constant k_x discussed above in relation to SPP generation in the R-SPP system (structure 1) should correlate, under appropriate circumstances, with propagation constants of certain of the allowed TM modes of the four-layer slab (structure 2 of Fig. 1). The modes, for a given optical frequency ω, are defined as solutions of Maxwell's equations satisfying the appropriate continuity boundary conditions at each interface and having purely outgoing character in outer layers 1 and 3 of Fig. 1.[15,17,20] We use Yeh's matrix method[17] to calculate the propagation constants $k_x=\beta+i\alpha$ associated with the allowed TM modes of structure 2. There can be a number of possible k_x solutions for a given frequency ω, and we calculate and discuss the dispersion curves $\omega(\beta)$. We also determine field profiles associated with the modes.

Since the modal dispersion calculations for Fig. 4 involve a range of frequencies or wavelengths, the metal dielectric constant is taken to be a Drude plus two Lorentzian ($D+2L$) model, as used in Ref. 21, fit over a larger range of frequencies. The results are essentially the same as the Drude model of Sec. II A for $\lambda_0=532$ nm ($\varepsilon_{\mathrm{Ag}}^{D+2L}=10.2+i0.62$ compared to the Drude value, $\varepsilon_{\mathrm{Ag}}=-10.1+i0.84$, given above) but are more realistic away from 532 nm. Appendix outlines additional technical details of how we determine the modal solutions.

III. RESULTS AND DISCUSSION

In Fig. 2, we show the time averaged FDTD electric field intensities $\langle|\mathbf{E}|^2\rangle_t$ for several glass core thicknesses. In Fig. 2(a), $d=\infty$ (no bottom air layer), corresponding to standard Kretschmann–Raether SPP excitation.[1] In Fig. 2(b), $d=0$ so that the propagation region ($x>10$ μm) corresponds to a symmetric LR-SPP structure. The structures in Figs. 2(c)–2(g) have finite values of d and are consistent with the R-SPP picture of increased propagation lengths relative to the standard case. As noted in the Introduction, the simplest explanation of the effect is that radiation emitted by the SPP back down into the glass layer, which would normally be lost, is reflected back up to the propagation region owing to it encountering the lower glass and/or air interface. This reflected light hits the propagation region at the appropriate angle for regenerating more SPPs.[9] The structures in Figs. 2(d)–2(g) involve core thicknesses considerably larger than those considered in Ref. 9.

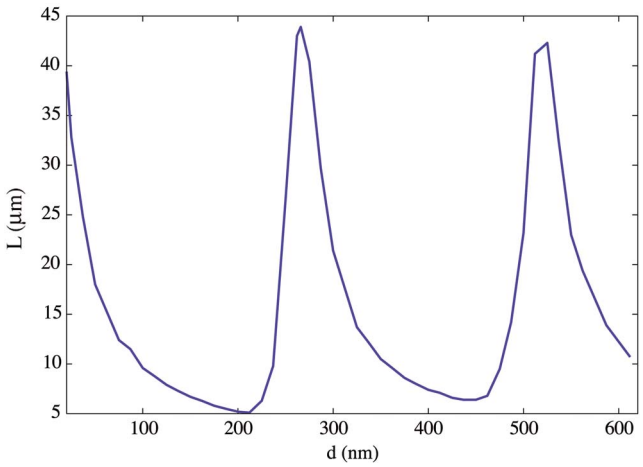

FIG. 3. (Color online) Plot of propagation length $L_x(d)$ as a function of the glass core thickness d, where L_x is determined from the FDTD results just above the metal film in the propagation region, as discussed in Sec. II A.

In Fig. 3, we plot of the R-SPP propagation length L_x determined from our FDTD results as discussed in Sec. II A, for each value of d considered. An interesting oscillatory dependence in $L_x(d)$ is seen, with maxima of ≈ 52 μm and minima of ≈ 5 μm. For comparison, the propagation length with the standard Kretschmann–Raether setup is just $L_x(d=\infty)=1.7$ μm. Thus, depending on the core thickness, propagation length enhancements up to 30 are possible.

It is natural suspect that the oscillations in Fig. 3 are due to excitation of system waveguide modes. Modal calculations for the allowed TM modes as a function of angular frequency for fixed values of glass thickness d were therefore performed (see Sec. II and Appendix for details). We show in Fig. 4 the resulting dispersion relations, $\omega(\beta)$ (symbols) for (a) $d=0$ nm, (b) $d=210$ nm, (c) $d=263$ nm, (d) $d=440$ nm, and (e) $d=518$ nm. Solid lines corresponding to the relevant air and glass light lines are indicated, and a horizontal solid line corresponding to $\omega_0=3.542\times10^{15}$ Hz, or $\lambda_0=532$ nm, is also shown. It is apparent that as d is increased, more modes become available. Most of these modes lie between the air (upper) and glass (lower) light lines and thus correspond to evanescent modes at the air and/or metal interface. The dispersion of one mode, however, can lie below both light lines. As d increases, this mode correlates even more with an evanescent mode on the metal and/or glass interface (i.e., the glass-side SPP) and is not relevant to our discussion of propagation lengths on the air side. The relevant TM modes between the air and glass lines are labeled TM_0, TM_1, TM_2, etc., and for fixed ω, $\beta(\mathrm{TM}_0)>\beta(\mathrm{TM}_1)>\beta(\mathrm{TM}_2)$, etc.

For $d=0$ [Fig. 4(a)], i.e., the air-metal-air case, two limits are considered. In the *thick metal slab* limit, represented here by $t_m=500$ nm (symbols connected by lines), there are two degenerate TM modes. In the *thin metal slab* limit, repre-

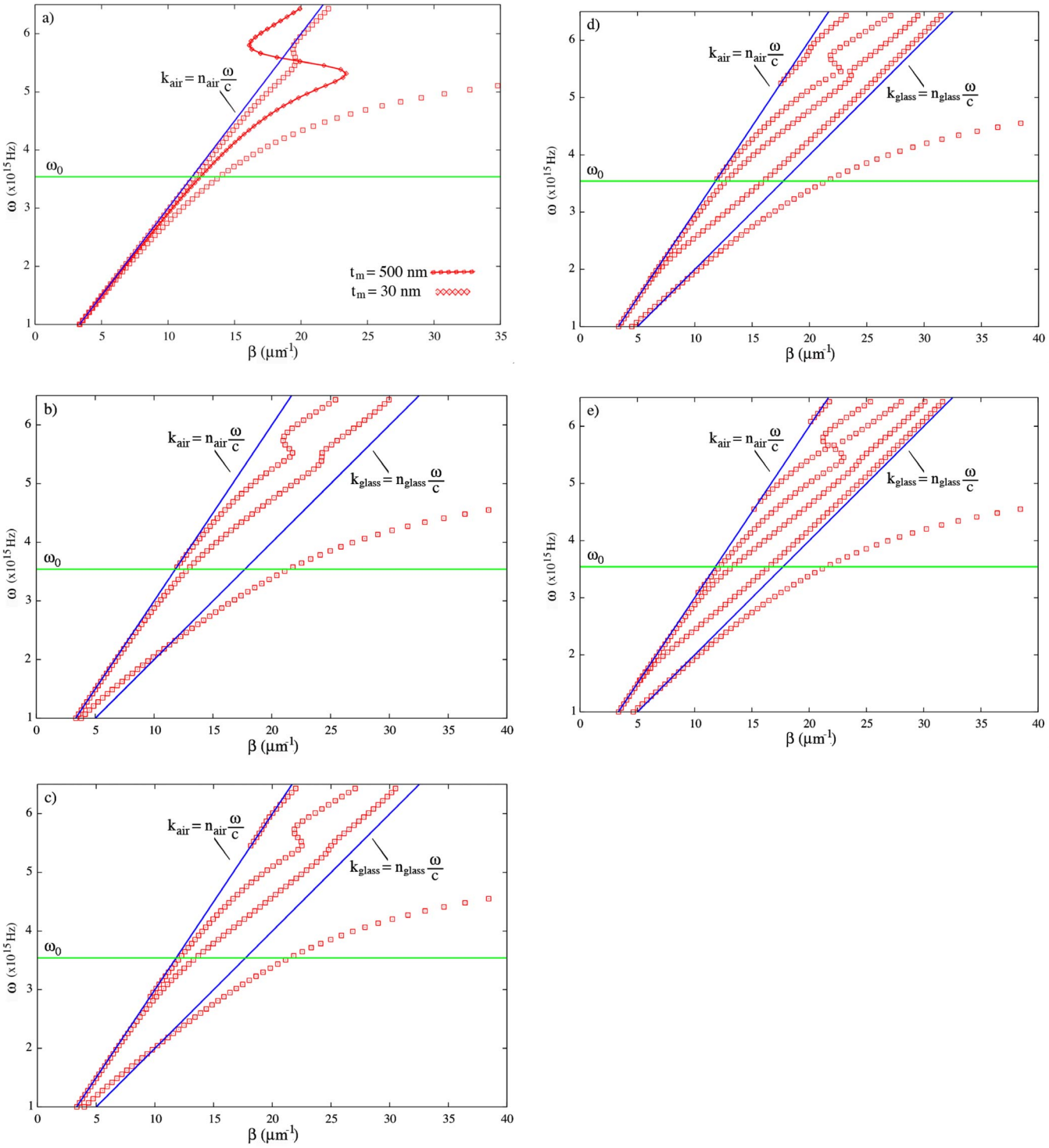

FIG. 4. (Color online) Dispersion curves for the waveguide structure given in Fig. 1(b), with (a) d=0 nm, (b) d=210 nm, (c) d=263 nm, (d) d=440 nm, and (e) d=518 nm calculated using Yeh's matrix method. The relevant air and glass light lines, as well as a horizontal line corresponding to $\omega_0 = 3.543 \times 10^{15}$ Hz, or λ_0=532 nm, are also shown.

sented by t_m=30 nm (symbols), the two degenerate modes begin to interfere and split, giving rise to symmetric, LR-SPP mode (smaller β) and a short lived, asymmetric mode (larger β).[15] For d=210 nm [Fig. 4(b)], only the TM_0 mode exists between the air and glass light lines along the horizontal line corresponding to λ_0=532 nm. However, by d=518 nm [Fig. 4(e)], there are now three possible modes, TM_0, TM_1, and TM_2, between the light lines along the λ_0=532 nm horizontal line. In this case, the TM_0 mode (largest β) is closest to the glass light line and TM_2 is closest to the air light line.

In Fig. 5, we compare the FDTD results (solid line) and the modal calculation results (symbols). That is, for

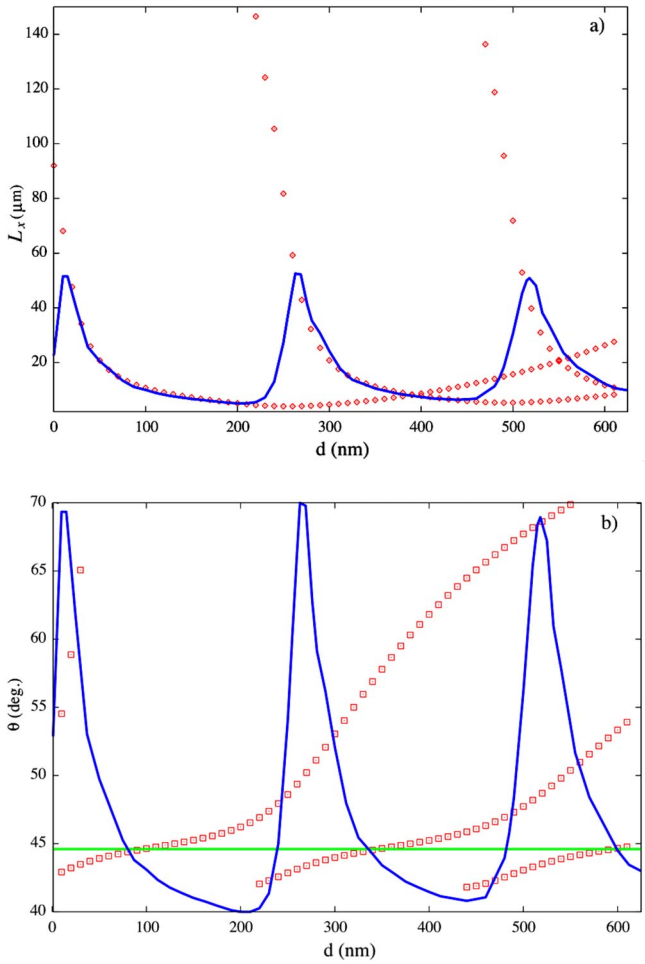

FIG. 5. (Color online) (a) Comparison of R-SPP propagation distances $L_x(d)$, with varying glass core thicknesses, inferred from the FDTD simulations (solid blue line) and waveguide modal analysis (symbols). (b) The ray angle θ (symbols) within the glass layer for a fixed wavelength $\lambda_0=532$ nm calculated with the modal analysis. The FDTD $L_x(d)$ curve (solid blue curve, not to scale) is also indicated for reference. The horizontal line corresponds to FDTD angle of incidence.

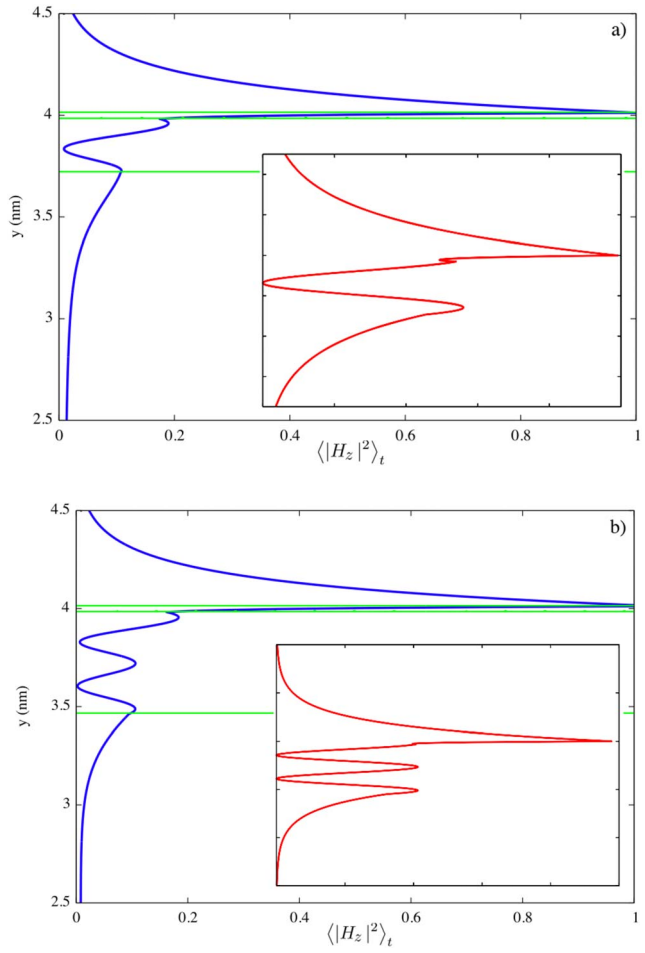

FIG. 6. (Color online) Profiles of the time-averaged H_z^2 inferred from our FDTD calculations (blue) and the modal profile inferred with the matrix method (inset red curve). (a) $d=263$ nm and (b) $d=518$ nm. Horizontal lines represent interfaces between layers. In each case, the maximum magnetic field intensity is set to 1 T^2.

$\lambda_0=532$ nm and for various values of d, we calculated $k_x=\beta+i\alpha$ and the ray angle θ within the glass layer. It is particularly striking that certain modal propagation lengths correlate extremely well with the FDTD propagation lengths [Fig. 5(a)]. As d increases, L_x for existing modes tends to decrease until the moment a new mode comes into existence. At this point, L_x becomes extremely large and then parallels the FDTD result. A consideration of Fig. 5(b) helps to explain this interesting correlation. Recall that the R-SPP incident excitation angle is fixed at $\theta_{SPP}=44.6°$. The modal propagation angles, i.e., the angles θ such that x component of the wave vector inside the glass layer is $\beta=n_{glass}(\omega_0/c)\sin(\theta)$, are generally $\theta\approx 42°$, just slightly below θ_{SPP}, when a given TM mode becomes first allowed but then increases with d. Optimal coupling into the given mode, with the incident light fixed at θ_{SPP}, thus occurs for d values slightly larger than threshold where $\theta\approx\theta_{SPP}$, and in Fig. 5, we see that this correlates very well with the observed maxima in $L_x(d)$ inferred from the FDTD calculations. Thus, with 532 nm light incident on the metal film from the glass at 44.6°, as ever thicker glass layers d, under the metal propagation region are considered, we have a picture of first the TM_0 mode (small d), then the TM_1 mode ($d\approx 263$ nm), and then the TM_2 mode ($d\approx 518$ nm) being efficiently coupled into by the light and leading to long range propagation.

We show the FDTD $\langle |H_z(y)|^2 \rangle_t$ profiles of the TM_1 mode for $d=263$ nm in Fig. 6(a), and the TM_2 mode for $d=518$ nm in Fig. 6(b), where $\langle |H_z(y)|^2 \rangle_t$ denotes the time average over one period as in Eq. (4). The inset in each case corresponds to the absolute square magnitude of the analogous modal result (see Appendix). As expected, the FDTD results are indeed consistent with excitation and propagation of an SPP tied into the TM_1 mode [Fig. 6(a)], which is characterized by one node in the glass region, and into the TM_2 mode [Fig. 6(b)] with two nodes in the glass region.

It is worthwhile noting that the field intensity profiles in Fig. 2 exhibit beating, indicative of multimodal excitation. This means that the excitation scheme involving the junction

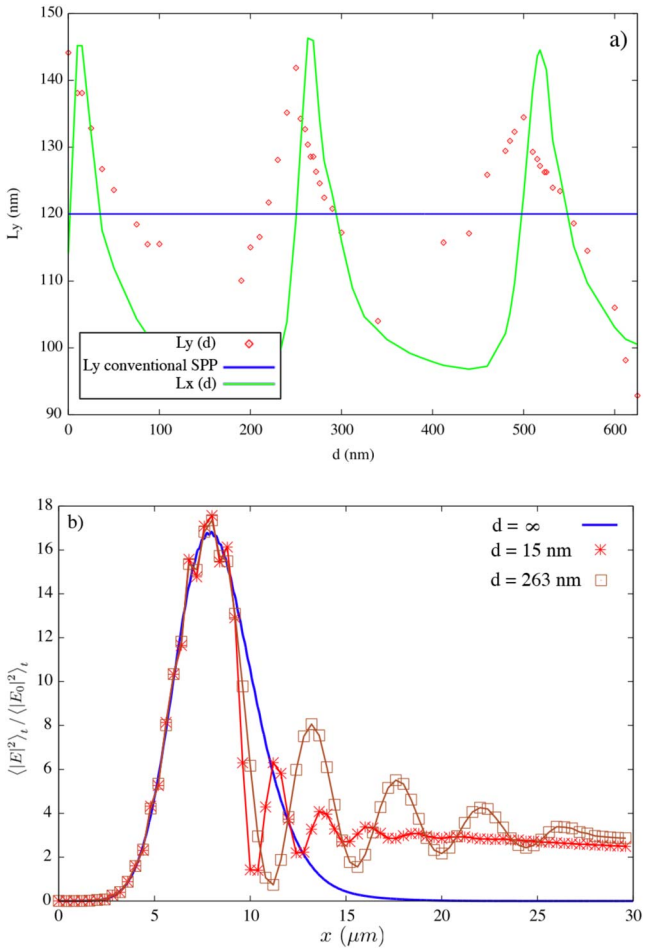

FIG. 7. (Color online) Surface confinement and intensity enhancement. (a) Air penetration depths L_y inferred from the FDTD calculations as a function of glass core thickness d. For reference, the lateral propagation distance $L_x(d)$ is also shown, not to scale. (b) Electric field intensity enhancements at a distance of 17 nm above the metal surface as a function of lateral displacement, x, for $d=\infty$, $d=15$ nm, and $d=263$ nm.

at $x \approx 9$ μm (see Fig. 1) excites more than one waveguide mode. Indeed, the dispersion curves of Fig. 4 show the existence of several possible modes for the incident wavelength we are considering. These modes (see Appendix) have different ray angles θ_2 in the glass layer of a system composed of layers 1/2/3/4=air/glass/metal/air. We can associate the R-SPP mode with the mode for which θ_2 is closest to θ_{SPP}, which is then consistent with the simple R-SPP mechanism introduced in Ref. 9. The incident light is also chosen to be at this angle to primarily couple into this mode. The effective propagation lengths in Fig. 3, however, can be somewhat less than the ideal R-SPP mode propagation lengths due to the excitation creating varying degrees of other modes with smaller propagation lengths.

While it is clear from Figs. 3–6 that increased propagation distances are possible in the asymmetric R-SPP waveguide structure to the credit of waveguide modes, additional characteristics are also important and need consideration. For example, it has been pointed out that LR-SPPs can be less confined to the metal surface than pure SPPs.[4] However, it is desirable from the point of view of some applications to maintain confinement. To assess the degree of confinement to the metal surface, we consider fixed values of x in the range of 10 to 15 μm and fit the y dependence of the FDTD time-averaged intensities, $\langle |E|^2 \rangle_t$, to $C' \exp(-y/L_y)$ for y values ranging from the metal and/or air interface to 600 nm above it in the air. The resulting air penetration depths L_y as a function of d are shown as symbols in Fig. 7(a). The corresponding propagation lengths along x and L_x are also shown as a solid curve (not to scale). It is evident that L_y for R-SPPs maintains confinement and fluctuates within $\pm 20\%$ the conventional SPP value, which is designated by the horizontal line.

Another important consideration is the degree of field intensity enhancement at the air and/or metal interface, since one might expect that exciting waveguide modes could unfavorably localize energy density within the core. In Fig. 7(b), we address this concern and show the field intensity enhancements, $\langle |E|^2 \rangle_t / \langle |E_0|^2 \rangle_t$, for $y=17$ nm above the metal surface for the conventional SPP case, $d=\infty$, and two R-SPP cases, $d=15$ nm and $d=263$ nm. (Similar enhancements are observed for $d=518$ nm but are not included as to avoid a proliferation of symbols.) The initial intensity enhancement in the excitation region is the same for the all cases and, moreover, the R-SPP intensity enhancements further down the propagation region can be orders of magnitude more intense than the conventional case. Note that the initial enhancement, $\approx 16-18$ in this case, could likely be increased if the metal thickness and angle of incidence were optimized.[1]

IV. CONCLUDING REMARKS

We presented a detailed study and analysis of SPP propagation enhancement in the R-SPP structure suggested by Lee and Gray.[9] We found that SPP propagation lengths L_x can enhance 30-fold at a variety of glass core thicknesses d. These propagation enhancements occur without significant loss of surface confinement and can involve significant intensity enhancements in the propagation region. We were able to understand these results in terms of a mechanism involving coupling into certain waveguide modes of the system.

More specifically, our study involved a fixed incident angle and wavelength, and we showed how an interesting oscillatory behavior in L_x as a function of d could be achieved. The maxima corresponded to efficient coupling into specific TM modes just as they become open. Conversely, one should also be able to excite such modes with their very long propagating SPPs for a fixed core thickness d by varying, for example, the incident angle. The wavelength (532 nm) and metal film (silver) examined were such that the conventional SPP propagation distances were on the order of 2 μm and the optimal R-SPP propagations were on the order of 50 μm. Longer incident wavelengths, e.g., telecommunication wavelengths of >1 μm, can have considerably longer conventional SPP propagation lengths, and the R-SPP approach can still be applied in such cases. In fact, our modal calculations suggest that enhanced propagation lengths can

indeed be obtained over a wide range of wavelengths. For example, for fixed thickness $d=263$ nm, incident wavelengths in the range of 700–1500 nm lead to propagation enhancements ranging from 5 to 50.

Our results significantly extend the original R-SPP idea and also should provide greater flexibility for the eventual fabrication of devices that utilize it. For example, the types of SPP and/or dielectric modes we have identified in the R-SPP system might also be usefully coupled into hole array systems as in Ref. 3.

ACKNOWLEDGMENTS

We thank Tae-Woo Lee for providing us with his FDTD code and giving advice on the implementation of Yeh's method. This work was supported by the Office of Basic Energy Sciences, Division of Chemical Sciences, Geosciences, and Biosciences, U.S. Department of Energy under Contract No. DE-AC02-06CH11357.

APPENDIX: MODAL ANALYSIS

We outline our implementation of Yeh's matrix method[17] to obtain dispersion curves and modal profiles of multilayer slab waveguide problems, focusing on the TM case of interest to this paper. In what follows, we use our coordinate system (Fig. 1), assume the convention that a forward moving plane wave in the x direction is of the form $\exp[+i(k_x x-\omega t)]$, and take the refractive index in a nonmagnetic absorbing medium to be of the form $n=n_R+in_I$, with n_R and $n_I>0$.

We assume N uniform layers in y, with x and z invariance, and an index profile given by

$$n=\begin{cases} n_1, & y<y_1 \\ n_2, & y_1<y<y_2 \\ \vdots & \\ n_N, & y>y_{N-1}, \end{cases} \tag{A1}$$

where the thickness of layer l is given by $d_l=y_l-y_{l-1}$. See, for example, structure 2 of Fig. 1. The plane of incidence is taken to be the x-y plane and the TM electromagnetic ($F=E_x,E_y$, or H_z) field components are assumed to be of the form

$$F(x,y,t)=F_m(y)\exp[i(k_x x-\omega t)]. \tag{A2}$$

While not explicitly stated in Ref. 17 the TM modal profiles in Eq. (A2) are

$$E_{x,m}(y)=\begin{cases} \{E_1^+\exp(ik_{y1}y)+E_1^-\exp(-ik_{y1}y)\}\cos(\theta_1), & y<y_1\equiv 0 \\ \{E_2^+\exp[ik_{y2}(y-y_1)]+E_2^-\exp[-ik_{y2}(y-y_1)]\}\cos(\theta_2), & y_1<y<y_2 \\ \vdots & \\ \{E_N^+\exp[ik_{yN}(y-y_{N-1})]+E_N^-\exp[-ik_{yN}(y-y_{N-1})]\}\cos(\theta_N), & y>y_{N-1}, \end{cases} \tag{A3}$$

$$E_{y,m}(y)=\begin{cases} \{E_1^+\exp(ik_{y1}y)-E_1^-\exp(-ik_{y1}y)\}\sin(\theta_1), & y<y_1\equiv 0 \\ \{E_2^+\exp[ik_{y2}(y-y_1)]-E_2^-\exp[-ik_{y2}(y-y_1)]\}\sin(\theta_2), & y_1<y<y_2 \\ \vdots & \\ \{E_N^+\exp[ik_{yN}(y-y_{N-1})]-E_N^-\exp[-ik_{yN}(y-y_{N-1})]\}\sin(\theta_N), & y>y_{N-1}, \end{cases} \tag{A4}$$

$$H_{z,m}(y)=\sqrt{\frac{\varepsilon_0}{\mu_0}}\begin{cases} n_1\{E_1^+\exp(ik_{y1}y)-E_1^-\exp(-ik_{y1}y)\}, & y<y_1\equiv 0 \\ n_2\{E_2^+\exp[ik_{y2}(y-y_1)]-E_2^-\exp[-ik_{y2}(y-y_1)]\}, & y_1<y<y_2 \\ \vdots & \\ n_N\{E_N^+\exp[ik_{yN}(y-y_{N-1})]-E_N^-\exp[-ik_{yN}(y-y_{N-1})]\}, & y>y_{N-1}, \end{cases} \tag{A5}$$

where k_{yl} is the y component of the wave vector in layer l,

$$k_{yl}=\left[\left(n_l\frac{\omega}{c}\right)^2-k_x^2\right]^{1/2}=n_l\frac{\omega}{c}\cos(\theta_l), \tag{A6}$$

with $k_x=\beta+i\alpha$. The square root in Eq. (A6) is chosen to give positive imaginary components for k_{yl}. This condition is important for having evanescent decay in the outer layers for confined modes. The last equality in Eq. (A6) serves to formally define the angle θ_l, relative to the y axis, which is in general, complex valued. Equations (A3)–(A5) are formally consistent with Snell's law and are also properly interrelated by the vectorial Maxwell equations ($-i\omega n^2\varepsilon_0\mathbf{E}=\nabla\times\mathbf{H}$ and $i\omega\mu_0\mathbf{H}=\nabla\times\mathbf{E}$).

The requirement that the tangental components (E_x and H_z) be continuous at the interfaces leads to the following equations to determine the $\{E_l^{\pm}\}$ (Ref. 17):

$$\begin{pmatrix} E_1^+ \\ E_1^- \end{pmatrix}=D_1^{-1}D_2\begin{pmatrix} E_2^+ \\ E_2^- \end{pmatrix}, \tag{A7}$$

$$\begin{pmatrix} E_l^+ \\ E_l^- \end{pmatrix} = P_l D_l^{-1} D_{l+1} \begin{pmatrix} E_{l+1}^+ \\ E_{l+1}^- \end{pmatrix} \quad \text{for } l = 2,3,\ldots,N-1, \tag{A8}$$

with

$$D_l = \begin{pmatrix} \cos(\theta_l) & \cos(\theta_l) \\ n_l & -n_l \end{pmatrix} \tag{A9}$$

and

$$P_l = \begin{pmatrix} \exp(-ik_{yl}d_l) & 0 \\ 0 & \exp(ik_{yl}d_l) \end{pmatrix}. \tag{A10}$$

A confined waveguide mode is one for which field amplitudes go to zero as $y \to \pm\infty$. Therefore, the main goal is to solve for $k_x = \beta + i\alpha$ such that $E_1^+ = E_N^- = 0$. This modal condition is expressed as

$$\begin{pmatrix} 0 \\ E_l^- \end{pmatrix} = D_0^{-1}\left[\prod_{l=2}^{N-1} D_l P_l D_l^{-1}\right] D_{l+1} \begin{pmatrix} E_N^+ \\ 0 \end{pmatrix} = \begin{pmatrix} M_{11} & M_{12} \\ M_{21} & M_{22} \end{pmatrix} \begin{pmatrix} E_N^+ \\ 0 \end{pmatrix}, \tag{A11}$$

or, equivalently, $M_{11} = 0$. The dispersion curves in Fig. 4 are obtained by numerically searching the two-dimensional (β, α) parameter space for the roots of $M_{11} = 0$ for each ω of interest. We accomplish this with a simplex minimization procedure[22] designed to find the minima of the function

$$f(\beta, \alpha) = \{\mathrm{Re}(M_{11})\}^2 + \{\mathrm{Im}(M_{11})\}^2, \tag{A12}$$

and accepting as modal solutions only those minima that are zero to within machine precision. The simplex procedure requires a routine for repeatedly evaluating M_{11} for different points in the parameter space. For an arbitrary number of layers N, M_{11} is most easily obtained each time it is desired by evaluating the full M matrix using the various matrix multiplications in Eq. (A11). For a given initial guess for β and α, the minimization procedure corresponds to a trajectory in the parameter space that converges upon one specific solution. However, several different modal solutions may exist at a given ω. To obtain all solutions, the simplex procedure is carried out a number of times with different random initial guesses for β and α. For a given solution, the modal profiles in Fig. 6 of the text correspond to $|H_{z,m}|^2$ using $H_{z,m}$ from Eq. (A5).

[1] H. Raether, *Surface Plasmons on Smooth and Rough Surfaces and Gratings* (Springer, Berlin, 1988).
[2] J. Himola, Anal. Bioanal. Chem. **377**, 528 (2003).
[3] M. E. Stewart, N. H. Mack, V. Malyarchuk, J. A. N. T. Soares, T.-W. Lee, S. K. Gray, R. G. Nuzzo, and J. A. Rogers, Proc. Natl. Acad. Sci. U.S.A. **103**, 17143 (2006).
[4] J. Dostalek, A. Kasry, and W. Knoll, Plasmonics **2**, 97 (2007).
[5] W. L. Barnes, A. Dereux, and T. W. Ebbesen, Nature (London) **424**, 824 (2003).
[6] M. Hochberg, T. Baehr-Jones, C. Walker, and A. Scherer, Opt. Express **12**, 5481 (2004).
[7] S. Bozhevolnyi, V. S. Volkov, E. Devaux, J.-Y. Laluet, and T. W. Ebbesen, Nature (London) **440**, 508 (2006).
[8] D. Sarid, Phys. Rev. Lett. **47**, 1927 (1981).
[9] T.-W. Lee and S. K. Gray, Appl. Phys. Lett. **86**, 141105 (2005).
[10] T. Holmgaard and S. I. Bozhevolnyi, Phys. Rev. B **75**, 245405 (2007).
[11] J. A. Dionne, L. A. Sweatlock, H. A. Atwater, and A. Polman, Phys. Rev. B **72**, 075405 (2005).
[12] A. E. Craig, G. A. Olsen, and D. Sarid, Opt. Lett. **8**, 380 (1983).
[13] T. Nikolajsem, K. Leosson, I. Salakhutdinov, and S. I. Bozhevolnyi, Appl. Phys. Lett. **82**, 668 (2003).
[14] R. Charbonneau, P. Berini, E. Berelo, and E. Lisicka-Shrzek, Opt. Lett. **25**, 844 (2000).
[15] J. J. Burke, G. I. Stegeman, and T. Tamir, Phys. Rev. B **33**, 5186 (1986).
[16] A. Taflove and S. C. Hagness, *Computational Electrodynamics: The Finite-Difference Time-Domain Method*, 3rd ed. (Artech House, Boston, 2005).
[17] P. Yeh, *Optical Waves in Layered Media* (Wiley, New York, 1988).
[18] S. K. Gray and T. Kupka, Phys. Rev. B **68**, 045415 (2003).
[19] D. W. Lynch and W. R. Hunter, in *Handbook of Optical Constants of Solids*, edited by E. D. Palik (Academic, Orlando, 1985), pp. 350–357.
[20] G. Kovacs, in *Electromagnetic Surface Modes*, edited by A. D. Boardman (Wiley, New York, 1982).
[21] T.-W. Lee and S. K. Gray, Opt. Express **13**, 9652 (2005).
[22] J. P. Chandler, Behav. Sci. **14**, 81 (1969).